Sensitivity of MJO to the CAPE lapse time in the NCAR CAM3

Ping Liu, Bin Wang
International Pacific Research Center, University of Hawaii at Manoa, 1680 East-West RD, Honolulu, HI 96822

Gerald A. Meehl
National Center for Atmospheric Research, 1850 Table Mesa DR, Boulder, CO 80305

For J. Climate

Corresponding author address:
Dr. Ping Liu
International Pacific Research Center
University of Hawaii at Manoa
1680 East-West Road, Honolulu, HI 96822
Tel: 1-808-956-3305
Fax: 1-808-956-9425
E-mail: pliu@hawaii.edu

Abstract

Weak and irregular boreal winter MJO in the NCAR CAM3 corresponds to very low CAPE background, which is caused by easy-to-occur and over-dominant deep convection indicating the deep convective scheme uses either too low CAPE threshold as triggering function or too large consumption rate of CAPE to close the scheme. Raising the CAPE threshold from default 70 J/kg to ten times large only enhances the CAPE background while fails to noticeably improve the wind mean state and the MJO. However, lengthening the CAPE lapse time from one to eight hours significantly improved the background in CAPE and winds, and salient features of the MJO. Variances, dominant periods and zonal wave numbers, power spectra and coherent propagating structure in winds and convection associated with MJO are ameliorated and comparable to the observations. Lengthening the CAPE lapse time to eight hours reduces dramatically the cloud base mass flux, which prevents effectively the deep convection from occurring prematurely. In this case, partitioning of deep to shallow convection in MJO active area is about 5:4.5 compared to over 9:0.5 in the control run. Latent heat is significantly enhanced below 600 hPa over the central Indian Ocean and the western Pacific. Such partitioning of deep and shallow convection is argued necessary for simulating realistic MJO features. Although the universal eight hours lies in the upper limit of that required by the quasi-equilibrium theory, a local CAPE lapse time for the parameterized cumulus convection will be more realistic.

1. Introduction

The Madden-Julian oscillation (MJO; Madden and Julian 1971, 1972), a dominant mode of tropical atmospheric variability, peaks in power spectra at zonal wave numbers 1-3 and on time scale 30-60 days (e.g., Hendon and Salby 1994; Maloney and Hartmann 1998; Sperber 2003; Kiladis et al. 2005). Anomalies in winds and convection associated with MJO are closely coupled and propagate coherently eastward from the Indian Ocean to the Pacific at 5-10 m s^{-1}. Convective signal decays near the date line whereas the wind anomalies accelerate eastward. The disturbances are stronger in boreal winter than summer.

Realistic simulation and prediction of the MJO features have been challenging the state-of-the-art general circulation models (GCMs). Most GCMs produce MJO signals with much lower amplitude, shorter periods, and more irregular structure than observations (e.g., Slingo et al. 1996; Zhang 2005; Lin et al. 2006). In particular, the GCMs developed at the National Center for Atmospheric Research (NCAR) from the Community Climate Model Version 3 (CCM3) to the Community Atmospheric Model Version 2 (CAM2) have been simulating the MJO with extremely weak intensity and irregular structures. Similar to the CCM3 (Maloney and Hartmann 2001; Zhang and Mu 2005) and CAM2 (Sperber 2004; Liu et al. 2005) the latest version of CAM3 (Mu and Zhang 2006; section 3) produces the MJO variance and power spectra about one tenth of the observed in zonal winds, outgoing long-wave radiation (OLR), and precipitation. The simulated MJO has a standing structure corresponding to less realistic low-level zonal wind and low thermodynamic background.

The MJO simulation is sensitive to the convective parameterizations implemented in GCMs. Same GCM incorporated with different convective schemes can produce distinct MJO features. Wang and Schlesinger (1999) tested a GCM with three convective parameterizations: a modified Arakawa–Schubert scheme (Arakawa and Schubert 1974), the Kuo scheme (Kuo 1974), and the Manabe scheme (Manabe et al. 1965). Remarkably different MJO spectra were generated by these schemes. Maloney and Hartmann (2001) demonstrated that the CCM3 can enhance the MJO in amplitude and power spectra by implementing the relaxed Arakawa–Schubert scheme in contrast to the Zhang and McFarlane scheme (ZM95; Zhang and McFarlane 1995) and the Hack scheme (Hack 1994). On the other hand, different GCMs incorporating same convective scheme can produce contrastable MJO features and demonstrate distinct sensitivity to some important aspect of the scheme. For example the relative humidity threshold was found important to the MJO in the modified Arakawa-Schubert scheme as shown by Wang and Schlesinger (1999). As the threshold increases, the MJO becomes stronger. Maloney and Hartmann (2001), however, demonstrated that the relative threshold is not important in the relaxed Arakawa-Schubert scheme whereas an elevated threshold produces an even weaker MJO.

The simulation of MJO is also sensitive to the closure condition of convective schemes and the results are not all in agreement. Slingo (Slingo et al. 1996) compared fifteen GCMs and showed that convective schemes closed on local vertical stability produce a more realistic MJO than others closed on moisture convergence. Liu et al. (2005), however, showed that the Tiedtke convective scheme (Tiedtke 1989) incorporated in the CAM2 generates a more realistic MJO when closed on moist convergence than buoyancy. These sensitivity results suggest that the simulation of MJO is highly model- and scheme-dependent. Either single-model-multi-scheme or multi-model-single-scheme scenario is able to disclose the deficiencies in a GCM while provides limited insightful clues for the improvement of a specific scheme for the MJO simulation. The investigation of one scheme in one GCM may shed light on such improvement.

The weak and irregular MJO in the NCAR GCMs can be attributed to the ZM95 convective scheme as similarly weak MJO also appears in the Canadian Climate Model (Sheng 1995) using the same scheme. Recently, when a modified closure for the ZM95 scheme is employed in the CCM3 (Zhang and Mu 2005) and CAM3 (Mu and Zhang 2006), the simulated MJO is improved with enhanced amplitude and in eastward propagation. However, the signal still has a much shorter period and smaller spatial scale than that observed, which is disclosed as a common problem in GCMs by Slingo (Slingo et al. 1996; Lin et al. 2006). The modified closure (Zhang 2002) in the ZM95 considers the CAPE tendency solely from free atmosphere excluding the contributions by boundary processes, which is not consistent with the original quasi-equilibrium assumption of Arakawa and Schubert (1974) and observational evidence therein. Excluding surface processes in producing CAPE tendency in the tropical area can be even arguable where surface fluxes are essential to build up convective instability. The validation of this new closure assumption in the MJO active areas, however, is beyond the scope of current study. There can be other important aspects of the ZM95 scheme that contribute to the poor simulation of MJO.

Dai and Trenberth (2004) disclosed that the coupled version of CAM2 produces an unrealistic diurnal cycle. There is little CAPE accumulation in the morning and early afternoon due to premature initiation of deep convection, which prevents intense convection from occurring in the mid to late afternoon. As a result the precipitation occurs too frequently at reduced intensity despite the fairly realistic patterns of rainy days. Because deep convection removes atmospheric moisture prematurely, the ratio of convective versus non-convective precipitation is too high. Such dominant and premature deep convection indicates either the triggering function is extremely easy to reach or the CAPE consumption is too fast in the ZM95 scheme.

This study is intended to investigate whether the simulation of MJO in CAM3 is sensitive

to the CAPE threshold and consumption rate. Section 2 reviews the CAM3 and ZM95 with experimental design. Section 3 presents sensitivity of simulated background and MJO variances. Section 4 demonstrates that salient features in a composite MJO life cycle can be significantly improved and comparable to that observed when the CAPE lapse time is changed to eight hours. Section 5 reasons the improvement by showing the changes in partitioning of deep, shallow and stratiform precipitations, and vertical heating structures along the equatorial belt in the eight-hour case. Discussions and summaries are presented in section 6.

2. CAM3, ZM95 and experimental design

2.1 CAM3

The Community Atmospheric Model version 3 (CAM3) is the latest GCM developed at the National Center for Atmospheric Research (NCAR). A series of significant changes have been made during the past decade. Treatment of cloud condensed water deals more realistically with the condensation and evaporation under forcing by large scale processes and changing cloud fraction. A new thermodynamic package is implemented for sea ice to use the same physics for predicting snow depth, brine pockets, internal shortwave radiative transfer, surface albedo, ice-atmosphere drag, and surface exchange fluxes. Fractional land and sea-ice coverage are explicitly represented. A new, general, and flexible treatment of geometrical cloud overlap is used in the radiation calculations. The shortwave and longwave fluxes and heating rates are computed for random overlap, maximum overlap, or an arbitrary combination of maximum and random overlap. A new parameterization for the longwave absorptivity and emissivity of water vapor preserves the formulation of the radiative transfer equations using the absorptivity/emissivity method. The uniform background aerosol has been replaced with a present-day climatology of sulfate, sea-salt, carbonaceous, and soil-dust aerosols. These aerosols affect the shortwave energy budget of the atmosphere. Detail information about this model is referred to Collins et al. (2006).

2.2 ZM95 scheme

The NCAR GCMs since CCM3 have incorporated the ZM95 parameterization for deep moist convection, while shallow dry convection is treated using the Hack scheme. Rasch (2006) showed that the ratio of convective to stratiform precipitation is too high in the CAM3. As sampled in this study and shown in Figure 1, the ZM95 scheme produces convective rainfall that takes over 90% of the total precipitation during boreal winter season in the equatorial Indian and Pacific Oceans where observed MJO peaks in convection. This extremely high percentage indicates that the convection is nearly all of deep-convection origin in the CAM3, which leaves very little share for the shallow and

the stratiform condensation due to grid saturation (not shown). Although it is hard to justify the real partitioning among the different types of precipitation, Rasch (2006) showed that stratiform precipitation in the tropics can take 15~50% of the total in the observations. There must be some aspects inappropriate in the ZM95 scheme so that it generates such high percentage of precipitation then probably the poor MJO.

Fig. 1 Percentage of deep convective precipitation to the total in CAM3 during DJFM season averaged from 1979 to 2001.

The ZM95 scheme is based on the quasi-equilibrium theory proposed by Arakawa and Schubert (1974). The theory predicts that convective instability is gradually built up by large-scale forcing and will be destroyed quickly by small-scale cumulus ensemble under favorable conditions so that the atmosphere stays in a series of quasi-equilibrium state. The time scale of large-scale processes is much larger than that of small-scale adjustment, which is the essence of the theory.

Historically, the triggering conditions and adjustment time are specified according to different assumptions in parameterizations. Arakawa and Schubert (1974) proposed that the triggering function can be any positive cloud work function or CAPE. According to Cheung (2004), the mean CAPE is 1184.1 J kg^{-1} for tropical cyclone formations in the Western North Pacific, which suggests that small positive CAPE can be too low for triggering deep convection. In GCMs, increasing the CAPE threshold can significantly impact the transients (Lin and Neelin 2000; Vitart et al. 2001). For example, the ECMWF Seasonal Forecasting System (Vitart et al. 2003) increases the CAPE threshold to 500 J kg^{-1} in the Tiedtke convective scheme (Tiedtke 1989), which leads to significant increase of energy in the 40-50 day band. The ZM95 scheme also assumes a positive CAPE as the triggering function although the CAPE includes small convective inhibition (CIN) below the level of free convection. The CAM3 uses 70 J kg^{-1} in CAPE as the threshold to trigger deep convection, which can be too low.

Arakawa and Schubert (1974) gave the adjustment time scale at the orders of 10^3~10^4 s (EQ 154 in their paper), which ranges from 15 minutes to 10 hours. The specified adjustment time represents the lifetime for the parameterized convection. Li et al. (2003) found that the tropical convection gains maximum perturbation kinetic energy about 4-5 hours before maximum decay of moist available potential energy. Meanwhile they showed that at least three hours are needed for the convection to reach maximum. Their results suggest that the lapse time of CAPE can be 4-8 hours.

The ZM95 scheme determines the cloud-base mass flux M_b as

$$M_b = \frac{A}{\tau \bullet F}, \tag{1}$$

where A, τ, and F are CAPE, CAPE lapse time, and CAPE tendency per unit M_b by large-scale processes, respectively. The M_b redistributes the mass fluxes of updrafts and downdrafts and closes the scheme. In the ZM95, the adjustment time τ is assumed as two hours which was used in the CCM3 and CAM2. The CAM3 CTL (Table 1) uses one hour that can be too short.

Fig. 2 Reversible CAPE (J kg^{-1}) in (a) ERA40 and (b) CAM3 CTL during DJFM averaged from 1979 to 2001. Contour is 200, ≥ 400 shaded.

According to the heat engine theory of Renno and Ingersoll (1995), pseudo-adiabatic CAPE should be at least 1000 J kg^{-1} in tropical area for compensating mechanical dissipation. Figure 2 shows long-term-mean reversible CAPE in DJFM season derived from the ECMWF Reanalysis-40 (ERA40) project and the CAM3 (see next section for CAPE calculation). The reversible CAPE in ERA40 is greater than 400 J kg^{-1} (shaded area in Figure 2a) in equatorial Indian to Pacific oceans while it is about 200 J kg^{-1} in CAM3 (Figure 2b). Such low CAPE in CAM3 indicates non-adequate buildup and insufficient thermo-dynamic background for the MJO. Sensitivity experiments based on the above evidence will be presented as follows.

2.3 Experiment design

The model used in this study is the CAM3.1 at spectral T42 (approximately 300 × 300 km^2) resolution. It has 26 vertical hybrid layers incorporated with the Eulerian dynamical core. Two types of sensitivity runs will be conducted: to raise the CAPE threshold for triggering the deep convection from 70 to 700 J kg^{-1} and to lengthen the CAPE lapse time from 1 to 10 hours. Table 1 lists the experiment name conventions. All runs start on September 1, 1978 and end on September 1, 2002. The observed monthly SST data is used to force the runs. In addition to the variables default to output, we sample CAPE on each time step using the method described in the next section before deep convection.

2.4 Observational data and methodology

a. Data

Six-hourly thermodynamic variables from September 1, 1978 to August 31, 2002 are derived from the ERA40 server for CAPE calculation. Six-hourly winds, convective and large-scale precipitation rate, and OLR from the ERA40 are used for MJO validation. Daily OLR data is derived from the NOAA satellite observation; and pentad precipitation is from the CMAP (Xie and Arkin 1997).

b. CAPE calculation

The method in Xu and Emanuel (1989) is employed for CAPE calculation. Both reversible and pseudo-adiabatic types of CAPE are derived. The starting level to calculate CAPE in ERA40 is the first level above surface. In the ZM95, however, the starting level is where the maximum moist static energy occurs in the planetary boundary layer. For consistence, the same code to derive the CAPE is incorporated in the CAM3 before the ZM95 scheme starts deep convection. The ZM95 CAPE calculation is still used for the runs to change the threshold.

c. Analysis methods

Pentad mean data are derived from the high-frequency reanalysis and the CAM3 output. Long-term mean is then subtracted to obtain anomalies which are filtered by a 20-80 day band pass filter. Variances, wave-number frequency power spectra, and lag regression of OLR and winds are derived from the filtered series for MJO comparison. Long-term mean in DJFM is computed for climatology. Individual variables will be explained when they are used.

3. Sensitivity in mean state, variances and power spectra

We first show the sensitivity in climatological CAPE. Raising the CAPE threshold to three times large (210 J kg^{-1}; not shown) does not significantly help improve the CAPE climatology (c.f. Figure 2b). The overall CAPE is still much smaller than that in the ERA40. When the CAPE threshold is raised to 700 J kg^{-1}, the CAPE background is significantly changed and comparable to that in ERA40 (Figure 3a) except for smaller values in north of Australia (c.f. Figure 2a). No significant change occurs in ZM2HR (not shown). Lengthening the CAPE lapse time from four to ten hours gradually enhances the CAPE background. In ZM8HR case (Figure 3b), the CAPE in the Eastern Hemisphere has a comparable spatial pattern but has much larger amplitude than that in ERA40. Figure 3 indicates the CAPE background is more sensitive to the CAPE lapse time than threshold.

Fig. 3 Same as Figure 2 but for (a) CAPE700 and (b) ZM8HR.

Climatological zonal wind at 850 hPa shows different sensitivity. The ERA40 zonal wind (not shown) has a westerly belt in DJFM along the southern equatorial flank in most of the Eastern Hemisphere. A 4 m s^{-1} center occurs from the eastern Indian Ocean to the western Pacific where MJO convection peaks. This westerly belt is important to the MJO development (e.g., Inness et al. 2003). Similar to CCM3 (Maloney and Hartmann 2001) and CAM2 (Liu et al. 2005), the CAM3 control run (not shown) produces the westerly belt that is narrower with eastern edge ending near 150^{o}E. The westerly center is about 2

m s^{-1} larger than that observed and is concentrated in the western Maritime continent. Little is changed when the CAPE threshold is raised to 700 J kg^{-1} (Figure 4a): both the center and the width are almost the same as those in the control run. Such narrower and stronger low-level westerly corresponds to a non-propagating MJO signal as shown below. Raising the CAPE lapse time to eight hours, however, significant changes the low-level zonal wind mean state (Figure 4b). In particular, the eastern edge extends near the date line and the center is reduced to 4 m s^{-1} comparable to that observed. Two small broken spots, however, occur in the central and eastern Indian Ocean, which is not observed in ERA40. The overall improved low-level westerly will support coherent eastward propagation of the MJO signals as shown below.

Fig. 4 850 hPa zonal wind (m s-1) in (a) CAPE700 and (b) ZM8HR during DJFM averaged from 1979 to 2001. Contour is 2, ≥ 0 shaded.

The MJO variance in precipitation is generally lower in GCMs than observed (e.g., Slingo 1996; Lin et al. 2006). Observed precipitation variance (CMAP; not shown) in boreal winter has two distinct centers: one is in the Indian Ocean extending south-westward from Sumatra; the other is in the equatorial western Pacific. Both centers have a magnitude of 30~45 mm^2 day^{-2}. These two centers correspond to the convective peaks in an MJO cycle. The CAM3 CTL (not shown) has about 5-10 mm^2 day^{-2} variance with no discernable center in the Indian and Western Pacific oceans. Such low variance in precipitation has occurred in CCM3 (Maloney and Hartmann 2001) and CAM2 (Liu et al. 2005). Raising the CAPE threshold to three times large changes the precipitation variance very little (not shown). The magnitude and distribution are very similar to the CTL. In CAPE700 case (Figure 5a), the variance is enhanced only in the panel from south Ben of Bengal to the South China Sea. The MJO variance in precipitation increases gradually by lengthening the CAPE lapse time from 2 to 10 hours. Figure 5b shows the ZM8HR case in which the variance is dramatically enhanced with similar patterns but much larger amplitude than the CMAP. Sensitivity of variance in 850 hPa zonal wind is similar to that of precipitation (not shown).

Fig. 5 Variance in 20-80-day filtered precipitation (mm2 day-2) in (a) CAPE700 and (b) ZM8HR during DJFM averaged from 1979 to 2001. Contour is 5, ≥ 20 shaded.

The dominance of MJO in propagating direction, zonal wave number, and time scale can be demonstrated in a wave number-frequency power spectra diagram. In ERA40 (not show), the power spectra in 850 hPa zonal wind have peaks at zonal wave number 1-3, on 30-60-day period, in the eastward propagation, and with a maximum of 0.08 m^2 s^{-2}. The CAM3 CTL (not shown) has power spectra of 0.01 m^2 s^{-2} spreading on a wide range of time period in both east and westward propagation, which is very much similar to CCM3 (Maloney and Hartmann 2001) and CAM2 (Liu et al. 2005). The power spectra are

improved little when the cape threshold is lifted to 700 J kg^{-1} (Figure 6a). The maximum amplitude becomes 0.02 m^2 s^{-2} spreading from 15 to 50 days in period and concentrating on zonal wave number one. Lifting the CAPE threshold does not enhance the MJO power spectra (c.f. Figure 4a). For the cases to lengthen the CAPE lapse time, however, the power spectra are gradually improved. In ZM8HR (Figure 6b), the power spectra are dominant at zonal wave number one for eastward propagation. Dominant period has two centers on 30 and 60 days with magnitudes of 0.6 – 0.7 m^2 s^{-2}, comparable to those in ERA40 (not shown). Power spectra in OLR (not shown) have similar sensitivity to the CAPE threshold and lapse time as in the 850 hPa zonal wind.

Fig. 6 Wave number power spectra in 850 hPa zonal wind (m^2 s^{-2}) in (a) CAPE700 and (b) ZM8HR during DJFM averaged from 1979 to 2001.

The sensitivity of MJO in eastward propagation can be further illustrated by a lag regression diagram in low-level filtered zonal wind. After the filtered 850 hPa zonal wind is averaged over 10^oN ~ 10^oS belt, the time series on each meridian are regressed on 150^oE for a 30-day lead and lag. An MJO signal in ERA40 (not shown) generally starts at day -30 in the western Indian Ocean, propagates eastward, reaches the reference point at day 0, then accelerates eastward after cross the date line, and finally returns to the origin to close the cycle in 45-50 days. A standing rather than propagating structure appears in the CAM3 CTL (not shown) as disclosed in the CCM3 and CAM2 simulations. The standing structure also occurs in the CAPE210 run (not shown). In the CAPE700 case (Figure 7a), a westward propagation signal is seen to the west of the date line; eastward propagation occurs to the east of the date line. This two-way propagation does not differentiate each other as seen in the wave number-frequency power spectra diagram (Figure 6a). In contrast, lengthening the CAPE lapse time can significantly improve the eastward propagation of MJO. For the ZM8HR case in Figure 7b, the shaded signal in lower part of the panel starts at day -30 in the western Indian Ocean, moves slowly eastward, reaches the reference point (150^oE) at day 0, accelerates eastward after crossing the date line, and returns to the origin at day 10-15. This full MJO signal is in very good agreement with that in ERA40, indicating the high sensitivity of the MJO to the CAPE lapse time in CAM3.

Fig. 7 Lag regression of filtered 850 hPa zonal wind on 155^oE (m s^{-1}) in (a) CAPE700 and (b) ZM8HR during DJFM averaged from 1979 to 2001. Contour is 0.5, ≥ 0 shaded.

4. A composite MJO life cycle in ZM8HR case

Observational studies (e.g., Hendon and Salby 1994; Kiladis et al. 2005) have disclosed that the MJO has a baroclinic structure in zonal wind anomalies at 850 hPa and 200 hPa. Boundary layer convergence leads convection and builds up moisture fostering

convection in the eastward propagation. Convection center is usually located above low-level westerly anomalies. These observed features have been demonstrated in a composite MJO life cycle (e.g., Maloney and Hartmann 1998; Sperber 2003). To further elucidate these features and functioning mechanism in the ZM8HR case, we next show a composite MJO life cycle using the methodology described in Maloney and Hartmann (2001) and Liu et al (2005). The difference here is that OLR rather than 850 hPa zonal wind is used for EOF analysis and event selection. Filtered pentad anomaly of OLR is averaged between 10^oN and 10^oS to obtain time series on each meridian along the equator. EOF analysis is then applied to the co-variance matrix of the series. The First two EOFs from NOAA observation and ZM8HR are shown in Figure 8.

Fig. 8 EOF 1 (solid) and 2 (dashed) of the filtered OLR pentad anomaly along the equator (averaged in 10oN~10oS) from (a) NOAA satellite observation and (b) ZM8HR case in CAM3

Observed EOF 1 (solid line in Figure 8a) has a sine structure in the Eastern Hemisphere. Its maximum is about 0.2 normalized units and is located near 80^oE; its minimum is near -0.2 normalized units and occurs in 150^oE that is the reference point for the lag regression in Figure 7. The first EOF returns back to zero near 150^oW, which ends convection signal as shown in Figure 11. Observed EOF 2 (dashed line in Figure 8a) has a cosine structure and the maximum occurs in $90\sim130^oE$. The first two EOFs in the ZM8HR case (Figure 8b) correspond well with the observations in the sine and cosine structures except for small difference in amplitude. The distinct structures in EOF 1 and 2 indicate the quadrature structure of the dominant MJO convection, which will be shown in the composite MJO life cycle.

An MJO index is defined as a linear combination of the first two principal components (PCs) of the EOf analysis. The combination is determined by the maximum lead in correlation coefficient(s) between the two PCs. For example, if PC1 leads PC2 with maximum coefficients at 1 and 2 pentads, the combination will be PC1 + PC2 ($t = t + 1$) + PC2 ($t = t + 2$) where t represents time. Based on the derived MJO index time series, events in boreal winter are selected for composite. Each selected event has consecutive phases 1 and 9 whose index value is below minus one standard deviation and phase 5 above one standard deviation. The time indices are recorded for each phase in the selected events. Using the time indices, composites in filtered OLR, winds at 200 hPa and 850 hPa, precipitation, and 1000 hPa convergence are derived phase by phase as in Liu et al. (2005). The observed MJO propagating structure and mechanism can be characterized selectively in the composite phases 4 and 5.

Fig. 9 Phase 4 of the composite MJO life cycle.

Figure 9 shows the MJO structure in the composite phase 4. A baroclinic distribution is

clearly seen in wind anomalies at 200 hPa (Figure 9a) and 850 hPa (Figure 9b) along the equatorial area. Specifically in the Indian Ocean where the MJO convection is near its mature phase in OLR and precipitation (dark shaded area in Figure 9a and 9b), westerly wind dominates at 200 hPa while easterly dominates at 850 hPa. Convergence at 1000 hPa fuels the convection and more importantly it extends farther east to the Maritime Continent than OLR and precipitation, similar to that in observations (not shown).

Fig. 10 Same as Figure 9 but for phase 5.

Figure 10 illustrates the situation in phase 5. Besides the baroclinic structure in 200 and 850 hPa winds, convergence at 1000 hPa moves up to the date line and precipitation disturbance of shallow-convection origin moves to the western Pacific. Both convergence and shallow convection lead the OLR and deep convection whereas convergence even leads the precipitation (Figure 10b). The observed frictional moisture convergence mechanism clearly functions in the western Pacific in this case. Shallow convection is shown important and needs to be realistically simulated for the MJO. In the Indian Ocean in both phases 4 and 5, centers of OLR (contours) are located more in westerlies than in easterlies at 850 hPa, indicating that the frictional moisture convergence mechanism also functions and is very similar to that observed (e.g., Maloney and Hartmann 1998). Precipitation centers (contours), however, are located more in easterlies than in westerlies at 850 hPa. This correspondence is observed in the CAM2 (Liu et al. 2005) with the Tiedtke convective scheme (Tiedtke 1989) where the authors argued that the wind induced surface heat exchange (WISHE; Emanuel 1987; Neelin 1987) functions for the MJO development. The different correspondence between the OLR and 850 hPa zonal wind during the MJO cycle can be demonstrated below in Figures 11 and 12.

Fig. 11 Composite MJO life cycle in observational OLR (shaded) and 850 hPa zonal wind (contour) with interval 0.5 m s^{-1}

Using the selected events described above, the composite phases in OLR and 850 hPa zonal wind are averaged along the equator between 10^{o}N and 10^{o}S. The nine phases are repeated once for a clear inspection in Figures 11 and 12. In the observations (NOAA OLR and ERA wind), the dark shaded OLR cycle (Figure 11) starts at phase 2 above 850 hPa easterlies, which is in agreement with observations (Sperber 2003) who uses different MJO index and composite technique. The OLR reaches the first maximum of 12 W m^{-2} at phase 5 near 90^{o}E; its most part lies in the westerly side. This maximum moves to about 105^{o}E near the end of phase 6 then weakens in the Maritime Continent. The OLR reaches the second maximum of 12 W m^{-2} at phase 7 near 125^{o}E; the maximum lies completely in the westerlies. This cycle ends at next phase 4 near 15^{o}W with a total of 12 phases roughly about 60 days. The zero line of 850 hPa zonal wind starts at phase 3 and ends at next phase 3 with a total of 10 phases roughly about 50 days. Such difference indicates

the faster propagation of 850 hPa zonal wind than OLR with a quadrature structure. These features have been disclosed in previous studies (e.g. Hendon and Salby 1995; Maloney and Hartmann 1998) using different composite techniques or low-level zonal wind as the event selector.

Fig. 12 Same as Figure 11 but for the ZM8HR case

The general figure in the ZM8HR case (Figure 12) is comparable to that observed while difference exists. The dark shaded OLR cycle starts at phase 2 near 50^{o}E in low-level easterlies. After one-phase break, it develops and reaches the first maximum of 12 W m^{-2} at phase 4 near 70^{o}E, about one phase earlier and 20^{o}E further westward than the observations (Figure 11). About two thirds of the maximum lie in 850 hPa westerlies, which is in part agreement with observations (Figure 11). The OLR disturbance moves eastward without apparently weakening in magnitude and reaches the second maximum of 12 W m^{-2} at phase 7 near 150^{o}E. In this span, most OLR centers lie in 850 hPa westerlies except for one at 130^{o}E occurs in the easterlies. Although it ends near phase 4 as in observations, the dark OLR cycle can reach 40^{o}W, much more eastward than that observed (Figure 11). The low-level zonal wind cycle in ZM8HR starts at phase 3 and ends near next phase 4, a little longer than that observed. Overall, the ZM8HR has significantly improved the MJO simulation and some deficiencies remain.

5. Partitioning of shallow and deep convection in ZM8HR

As stated in the introduction, previous studies have shown the sensitivity of MJO simulation to different convective schemes. The distribution of vertical heating structure from deep and shallow scheme has not been investigated. We will show here that the improved MJO in ZM8HR case can be attributed to the changed partitioning between deep and shallow convection, and associated vertical heating structure.

Fig. 13 Percentage of convective precipitation to the total in ZM8HR during DJFM season averaged from 1979 to 2001 for (a) deep ZM95 scheme and (b) shallow Hack scheme, ≥ 45% shaded.

Raising the CAPE threshold to 700 J kg^{-1} reduces the ratio of deep convection to the total precipitation to very small extent in the MJO active area (not shown). Lengthening the CAPE lapse time gradually reduces the ratio of deep convection meanwhile increases that of the shallow convection. In the ZM8HR case, deep convective precipitation is reduced to about 50% of the total precipitation in the MJO active area compared to the over dominance in CTL (Figure 1). Shallow convection (Figure 13b) increases up to 45%. The largest increase occurs in the Indian Ocean extending from Madagascar to Sumatra, and the Western Pacific. Both areas correspond to the maximum MJO convection as

discussed in Figures 9-12. The ratio of 5:4.5 in deep and shallow convection in the MJO active area is nearly ideal for the CAM3 to simulate realistic MJO features in variance, power spectra, eastward propagation, and dominant zonal wave number an period as shown in last section.

The changes in ratio also reflect in the vertical heating structure. Figure 14 shows the difference of total convective heating (shallow plus deep) between the ZM8HR and CTL in long-term-mean DJFM along the Equator (averaged between 10^oN and 10^oS). Compared to the CTL, the total convective heating in ZM8HR is increased below 550 hPa apparently in four areas. From west to east, the first increase occurs in 25~35^oE between 900 and 650 hPa with maximum magnitude of 1.5 K day^{-1}; the second in 55~100^oE between 970 and 550 hPa with 1 K day^{-1}; the third in 125~180^oE between 970 and 570 hPa with 2 K day^{-1}; and the fourth on 75^oW with 1.5 K day^{-1}. All these four increases are of shallow convective origin, which can be observed by the difference solely in shallow convective scheme (not shown). Small cooling lies in between these warming areas. The 500 hPa level, which is near the non-divergent layer, undergoes an apparent cooling of -2.5 K day^{-1} in the Eastern Hemisphere. This large cooling corresponds to the reduction of deep convection ratio shown in Figure 13 and apparent in the difference in solely deep convective scheme (not shown). Warming of 0.5-1 K day^{-1} occurs near 200 hPa level corresponding to the warming below 600 hPa. The column undergoes systematic cooling in 100^oE and 125^oE, indicating the latent heating is redistributed. Boundary layer warming along the Equator is about 2 K day^{-1}, which indicates the significant weakening in the deep convection since the ZM95 scheme models directly the impact on the boundary layer through downdrafts. Although the propagating signal in deep and shallow convection is too noisy to observe a coherent structure as in OLR and low-level zonal wind (not shown), the changes in the convective heating structure is important to simulate realistic MJO features. Such importance is also supported by the very small changes in vertical heating structure in CAPE700 case (not shown).

Fig. 14 Difference in total convective heating (deep + shallow, K day^{-1}), between ZM8HR and CTL during DJFM season averaged from 1979 to 2001 along the Equator (10^oN ~ 10^oS average). Contour interval is 0.5, ≥ 0 shaded.

6. Summaries and discussions

The NCAR GCMs have had great difficulties in simulating MJO features since CCM3. Although the simulation can be improved by using alternative schemes, why the default parameterizations have such great difficulties remains unresolved. A new closure assumption for the deep convective scheme by Zhang (2002) can help improve the simulation while deficiencies remain in the MJO signal. Since the new assumption needs

to justify in the MJO active areas, this study is intended to investigate other important factors responsible for the difficulties. Sampling results show that the deep convective precipitation is over dominant in the CAM3 so that the simulated thermodynamic background is too low and deficiencies occur in low-level zonal wind mean state. This over dominance tends to consume convective instability easily and fast. Hypotheses are proposed that the scheme uses either a too low threshold to trigger the convection or a too fast CAPE consumption rate. Sensitivity results indicate that it is the too fast CAPE consumption rate that contributes mainly to the deficiencies in the MJO simulation. To lengthen the CAPE lapse time to eight hours reduces the deep convection ratio, enhances the shallow convection, improves the mean state, and more importantly produces the MJO features comparable to observations. The CAPE threshold elevated to ten times large as the default does not significantly help improve the MJO simulation because it changes the ratio of convective precipitation and vertical heating structure to a small extent.

From the closure condition as in EQ (1), lengthening the CAPE lapse time to eight hours is equivalent to reduce the cloud base mass flux to one eighth. The cloud base mass flux then reduces the strength of updrafts, downdrafts, condensation, and latent heat release according to the functions for modeling the cumulus cloud as described in ZM95. Consequently, the ZM95 scheme needs to change the mass flux distribution particularly its strength as a starting point to produce realistic MJO simulations in the current NCAR GCM. In addition to change the CAPE lapse time, the mass flux can be adjusted by the CAPE tendency per unit cloud base mass flux (F in EQ 1), which has been demonstrated in Mu and Zhang (2006) by using the new closure assumption (Zhang 2002). A third possibility is to use fraction of the total CAPE in the closure condition for the cloud base mass flux, which is used in the Emanuel scheme (Emanuel 1991). The quasi-equilibrium theory and observations have justified that cumulus convection generally initiates and develops at relatively small region of a convectively unstable area. The size of this region, either specified as a universal value or modeled by some function, needs further investigation.

Although the CAPE lapse time of eight hours for the ZM95 scheme lies in the upper limit of that required by the quasi-equilibrium assumption, the universally specified value is not justified in nature. After the ZM95 scheme reduces the share of convective instability consumption, shallow convection is enhanced as shown in this study. According to the computation code in CAM3 at T42 resolution, the Hack scheme uses 0.5 hours as the adjustment time for shallow convection. Sensitivity of simulated climate and MJO to this time scale deserves further study. The specification of a universal adjustment for any shallow convection, however, needs to be justified. Either shallow or deep cumulus convection occurring in different locations may have its unique strength and life time. A local CAPE lapse time is more realistic and under investigation.

Acknowledgements

This study is partially supported by the DOE-NSF SciDAC project under number 0012862. Part of sensitivity experiments are carried out at the SDSC. The CliPAS project provides computing power for some of the small tests. Discussions with Kenneth Sperber, Phil Rasch, Jim Hack, Aiguo Dai, Warren M. Washington, Jialin Lin, Xiaoqing Wu, and In-Sik Kang are helpful to the investigation. The Reanalysis data is derived from the ERA40 server.

References

Arakawa, A., and W. H. Schubert, 1974: Interaction of a cumulus cloud ensemble with the large-scale environment, Part I. *J. Atmos. Sci.*, **31**, 474-701.

Cheung, K. K. W., 2004: Large-scale environmental parameters associated with tropical cyclone formations in the Western North Pacific. *J. Climate*, **17**, 466-484.

Collins, W. D, and Co-authors, 2006: The Formulation and Atmospheric Simulation of the Community Atmosphere Model Version 3 (CAM3). *J Climate*, **19**, 2144–2161.

Dai, A., and K. Trenberth, 2004: The diurnal cycle and its depiction in the Community Climate System Model. *J. Climate*, **17**, 930-951.

Emanuel, K. A., 1987: An air-sea interaction model of intraseasonal oscillation in the Tropics. *J. Atmos. Sci.*, **44**, 2324-2340.

Emanuel, K. A., 1991: A scheme for representing cumulus convection in large-scale models. *J. Atmos. Sci.*, **48**, 2313-2335.

Hack, J. J., 1994: Parameterization of moist convection in the National Center for Atmospheric Research community climate model (CCM2). *J. Geophys. Res.*, **99**, 5551-5568.

Inness, P. M., and Coauthors, 2003: Simulation of the Madden–Julian Oscillation in a coupled general circulation model. Part II: the role of the basic state. *J. Climate*, **16**, 365–382.

Hendon, H. H., and M. L. Salby, 1994: The life cycle of the Madden–Julian oscillation. *J. Atmos. Sci.*, **51,** 2225–2237.

Kiladis, G. N., K. H. Straub, and P. T. Haertel, 2005: Zonal and vertical structure of the Madden–Julian oscillation. *J. Atmos.Sci.*, **62,** 2790–2809.

Knutson, T. R., and K. M. Weickmann, 1987: 30–60 day atmospheric oscillations: Composite life cycles of convection and circulation anomalies. *Mon. Wea. Rev.*, **115**, 1407–1436.

Kuo, Y. H., 1974: Further studies of the parameterization of the influence of cumulus convection of large-scale flow. *J. Atmos. Sci.*, **31**, 1232–1240.

Li, X., C.-H. Sui, and K.-M. Lau, 2002: Interaction between tropical convection and its environment: An energetics analysis of a 2D cloud resolving simulation. *J. Atmos. Sci.*, **59**, 1712-1722.

Lin, J. L., and Coauthors, 2006: Tropical intraseasonal variability in 14 IPCC AR4 climate models. Part I: Convective signals. *J.Climate*, **19,** 2665–2690.

Lin, W.-B., and D. J. Neelin, 2000: Influence of a stochastic moist convective parameterization on tropical climate variability. *Geophys.Res. Lett.*, **27,** 3691–3694.

Liu, P., B. Wang, K. Sperber, T. Li, and G. A. Meehl, 2005: MJO in CAM2 with Tiedtke convective scheme. *J. Climate*, **18,** 3007–3020.

Madden, R. A., and P. R. Julian, 1971: Detection of a 40–50 day oscillation in the zonal wind in the tropical Pacific. *J. Atmos. Sci.*, **28**, 702–708.

----, and ----, 1972: Description of global-scale circulation cells in the tropics with a

40–50 day period. *J. Atmos. Sci.*, **29**, 1109–1123

Maloney, E. D., and D. L. Hartmann, 1998: Frictional moisture convergence in a composite life cycle of the Madden-Julian Oscillation. *J. Clim.*, **11**, 2387–2403.

Maloney, E. D., 2002: An intraseasonal oscillation composite life cycle in the CCM3.6 with modified convection. *J. Climate*, **15,** 964–982.

Maloney, E. D., and D. L. Hartmann, 1998: Frictional Moisture Convergence in a Composite Life Cycle of the Madden–Julian Oscillation. *J. Climate*, **11**, 2387–2403.

Maloney, E. D., and D. L. Hartmann, 2001: The Sensitivity of Intraseasonal Variability in the NCAR CCM3 to Changes in Convective Parameterization. *J. Climate*, **14**, 2015–2034.

Manabe, S., J. Smagorinsky and R. F. Strickler, 1965: Simulated climatology of a general circulation mode with a hydrologic cycle. *Mon. Wea. Rev.*, **93**, 769-798.

Mu, M. and G. J. Zhang, 2006: Energetics of Madden-Julian oscillations in the National Center for Atmospheric Research Community Atmosphere Model version 3 (NCAR CAM3). *J. Geophys. Res.*, **111**, D24112, doi:10.1029/2005JD007003.

Neelin, J. D., I. M. Held, and K. H. Cook, 1987: Evaporation wind feedback and low-frequency variability in the tropical atmosphere. *J. Atmos. Sci.*, **44**, 2341-2348.

Rasch, P. J., and co-authors, 2006: A characterization of tropical transient activity in the CAM3 atmospheric hydrologic cycle. *J. Climate*, **19**, 2222-2242.

Renno, N. O., and A. P. Ingersoll, 1996: Natural convection as a heat engine: A theory for CAPE. *J. Atmos. Sci.*, **53**, 572-585.

Sheng, J., 1995: The Madden-Julian oscillation in the Canadian Climate Centre general circulation model. *Climate Dyn.*, **12**, 125-140.

Slingo, J. M., and Coauthors, 1996: Intraseasonal oscillations in 15 atmospheric general circulation models: Results from an AMIP diagnostic subproject. *Climate Dyn.*, **12,** 325–357.

Sperber, K. R., 2003: Propagation and the vertical structure of the Madden-Julian Oscillation. *Mon. Wea. Rev.*, **131**, 3018–3037.

------, 2004: Madden-Julian variability in NCAR CAM2.0 and CCSM2.0. *Clim. Dyn.*, **23**, 259–278.

Tiedtke, M., 1989: A comprehensive mass flux scheme for cumulus parameterization in large-scale models. *Mon. Wea. Rev.*, **117**, 1779-1800.

Vitart, F., J. L. Anderson, J. Sirutis, and R. E. Tuleya, 2001: Sensitivity of tropical storms simulated by a general circulation model to changes in cumulus parametrization. *Quart. J. Roy. Meteor. Soc.* **127,** 25–51.

------, M. A. Balmaseda, L. Ferranti, and D. Anderson, 2003: Westerly wind events and the 1997/98 El Nino event in the ECMWF seasonal forecasting system: A case study. *J. Climate*, **16**, 3153-3170.

Wang, W., and M. Schlesinger, 1999: The dependence on convection parameterization of the tropical intraseasonal oscillation simulated by the UIUC 11-layer atmospheric

GCM. *J. Clim.*, **12**, 1423–1457.

Xie, P., and P. A. Arkin, 1997: Global precipitation: A 17-year monthly analysis based on gauge observations, satellite estimates, and numerical model outputs. *Bull. Amer. Meteor. Soc.*, **78**, 2539–2558.

Xu, K.-M, and K. A. Emanuel, 1989: Is the tropical atmosphere conditionally unstable? *Mon. Wea. Rev.*, **117**, 1471-1479.

Zhang, C., 2005: Madden-Julian oscillation. *Reviews of Geophysics*, **43, RG2003**, 1-36.

Zhang, G. J., and M. Mu, 2005: Simulation of the Madden–Julian Oscillation in the NCAR CCM3 using a revised Zhang–McFarlane convection parameterization scheme. *J. Climate*, **18**, 4046-4064.

-----, 2002: Convective quasi-equilibrium in midlatitude continental environment and its effect on convective parameterization, *J. Geophys. Res.*, **107**, 4220, doi:10.1029/2001JD001005.

-----, and N. A. McFarlane 1995: Sensitivity of climate simulations to the parameterization of cumulus convection in the Canadian Climate Centre general circulation model. *Atmos. Ocean*, *33*, 407-446.

Figure captions

Fig. 1 Percentage of deep convective precipitation to the total in CAM3 during DJFM season averaged from 1979 to 2001.

Fig. 2 Reversible CAPE (J kg^{-1}) in (a) ERA40 and (b) CAM3 CTL during DJFM averaged from 1979 to 2001. Contour is 200, ≥ 400 shaded.

Fig. 3 Same as Figure 2 but for (a) CAPE700 and (b) ZM8HR.

Fig. 4 850 hPa zonal wind (m s-1) in (a) CAPE700 and (b) ZM8HR during DJFM averaged from 1979 to 2001. Contour is 2, ≥ 0 shaded.

Fig. 5 Variance in 20-80-day filtered precipitation (mm2 day-2) in (a) CAPE700 and (b) ZM8HR during DJFM averaged from 1979 to 2001. Contour is 5, ≥ 20 shaded.

Fig. 6 Wave number power spectra in 850 hPa zonal wind (m^2 s^{-2}) in (a) CAPE700 and (b) ZM8HR during DJFM averaged from 1979 to 2001.

Fig. 7 Lag regression of filtered 850 hPa zonal wind on 155oE (m s-1) in (a) CAPE700 and (b) ZM8HR during DJFM averaged from 1979 to 2001. Contour is 0.5, ≥ 0 shaded.

Fig. 8 EOF 1 (solid) and 2 (dashed) of the filtered OLR pentad anomaly along the equator (averaged in 10oN~10oS) from (a) NOAA satellite observation and (b) ZM8HR case in CAM3

Fig. 9 Phase 4 of the composite MJO life cycle.

Fig. 10 Same as Figure 9 but for phase 5.

Fig. 11 Composite MJO life cycle in observational OLR (shaded) and 850 hPa zonal wind (contour) with interval 0.5 m s^{-1}

Fig. 12 Same as Figure 11 but for the ZM8HR case

Fig. 13 Percentage of convective precipitation to the total in ZM8HR during DJFM season averaged from 1979 to 2001 for (a) deep ZM95 scheme and (b) shallow Hack scheme, ≥ 45% shaded.

Fig. 14 Difference in total convective heating (deep + shallow, K day^{-1}), between ZM8HR and CTL during DJFM season averaged from 1979 to 2001 along the Equator (10^oN ~ 10^oS average). Contour interval is 0.5, ≥ 0 shaded.

Table captions:

Table 1 Sensitivity runs to change the ZM95 scheme based on CAM3.1 T42L26

Table 1 Sensitivity runs to change the ZM95 scheme based on CAM3.1 T42L26

Abbreviation	CAPE Threshold (J kg^{-1})	CAPE lapse time (hour)
CTL	70	1
ZM210	210	1
ZM700	700	1
ZM2HR	70	2
ZM4HR	70	4
ZM6HR	70	6
ZM8HR	70	8
ZM10HR	70	10

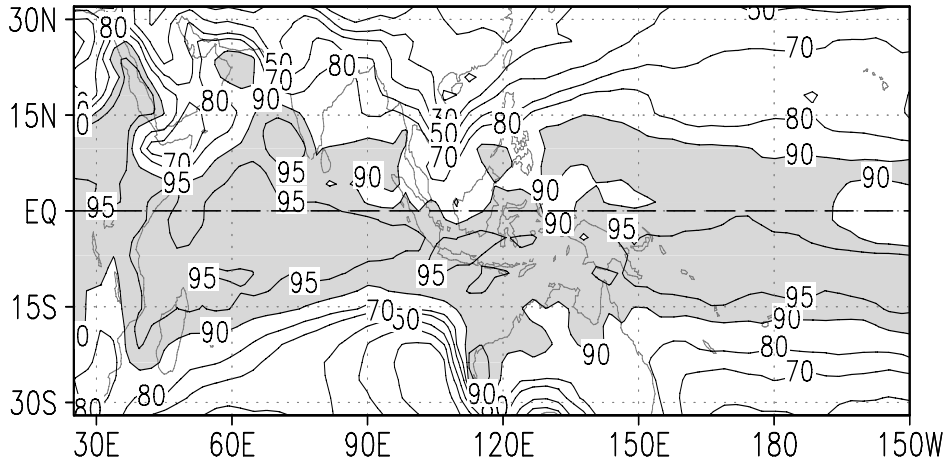

Fig. 1 Percentage of deep convective precipitation to the total in CAM3 CTL during DJFM season averaged from 1979 to 2001.

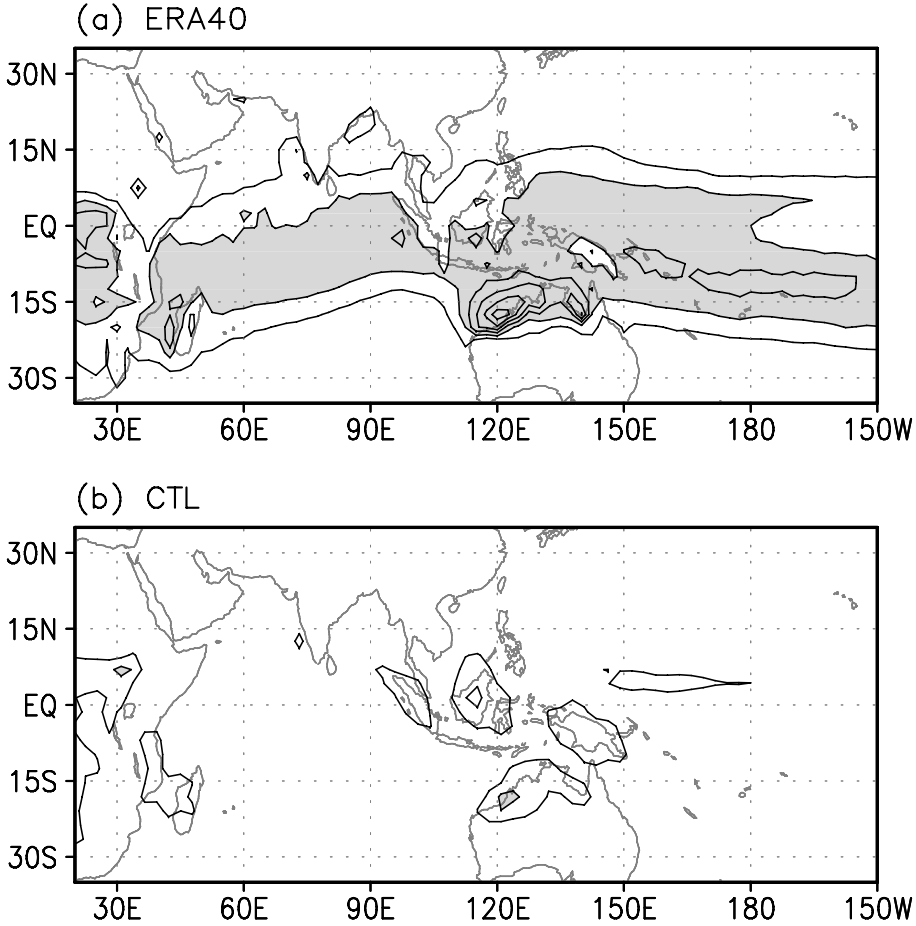

Fig. 2 Reversible CAPE (J kg^{-1}) in (a) ERA40 and (b) CAM3 CTL during DJFM averaged from 1979 to 2001. Contour is 200, ≥ 400 shaded.

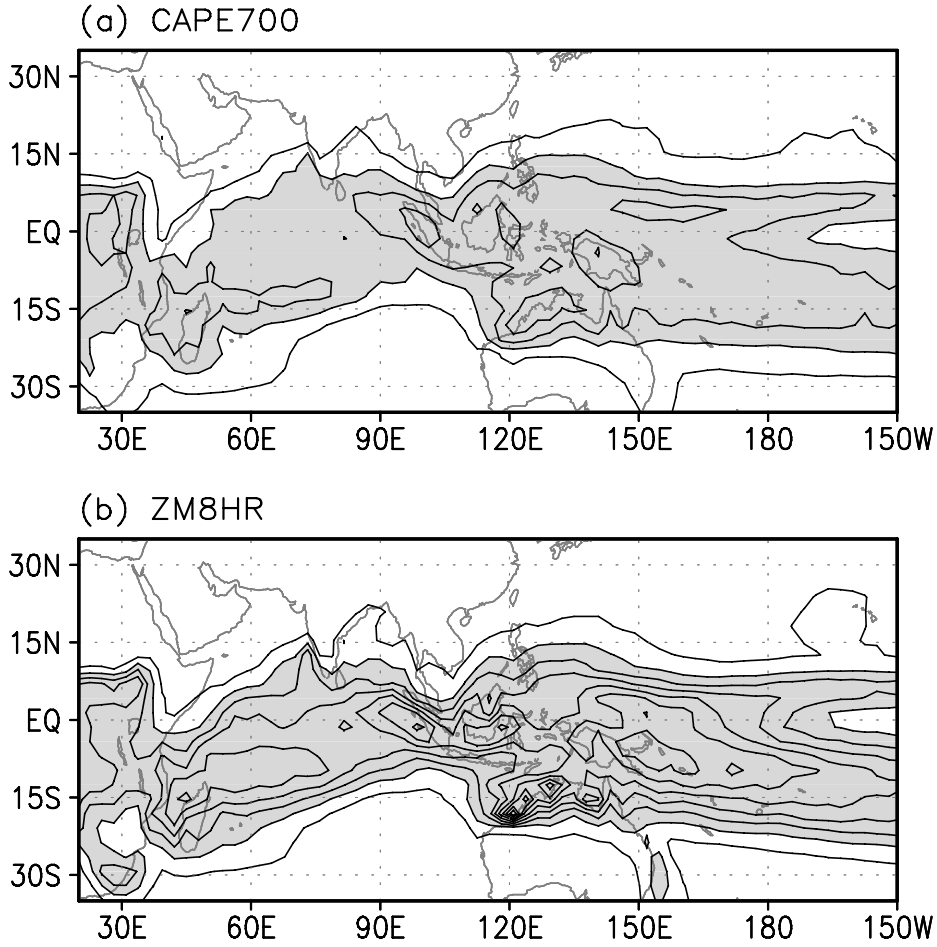

Fig. 3 Same as Figure 2 but for (a) CAPE700 and (b) ZM8HR.

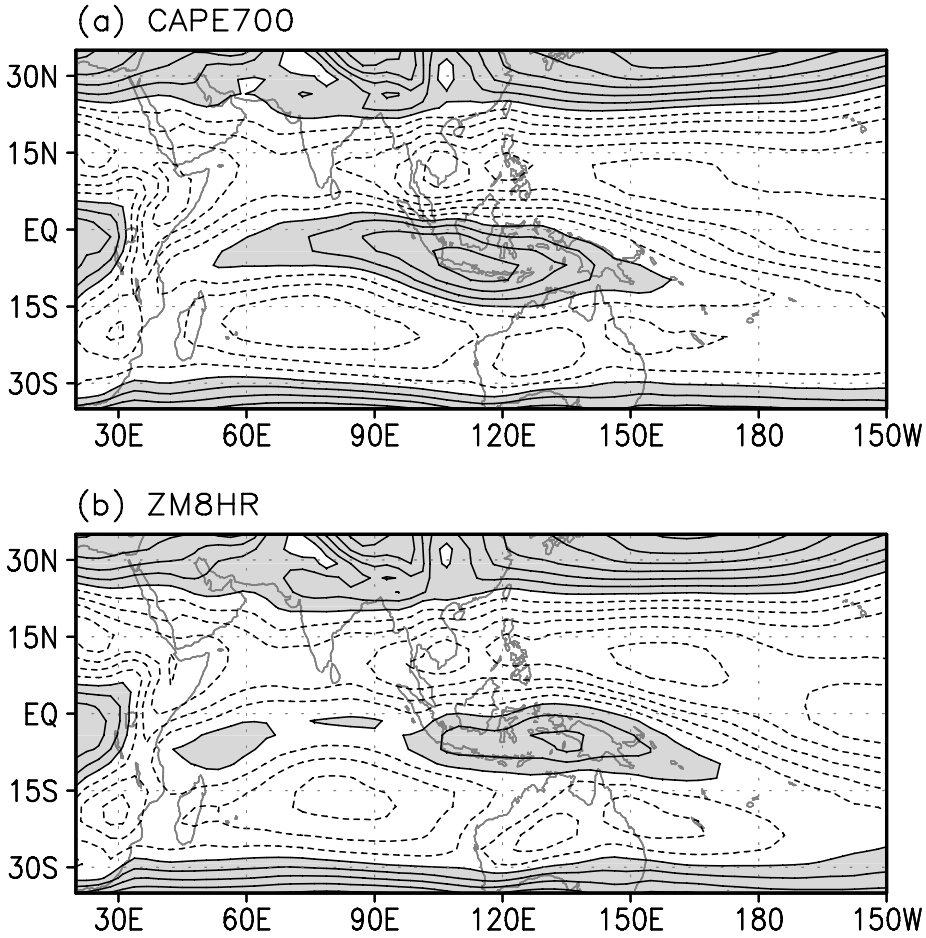

Fig. 4 850 hPa zonal wind (m s^{-1}) in (a) CAPE700 and (b) ZM8HR during DJFM averaged from 1979 to 2001. Contour is 2, ≥ 0 shaded.

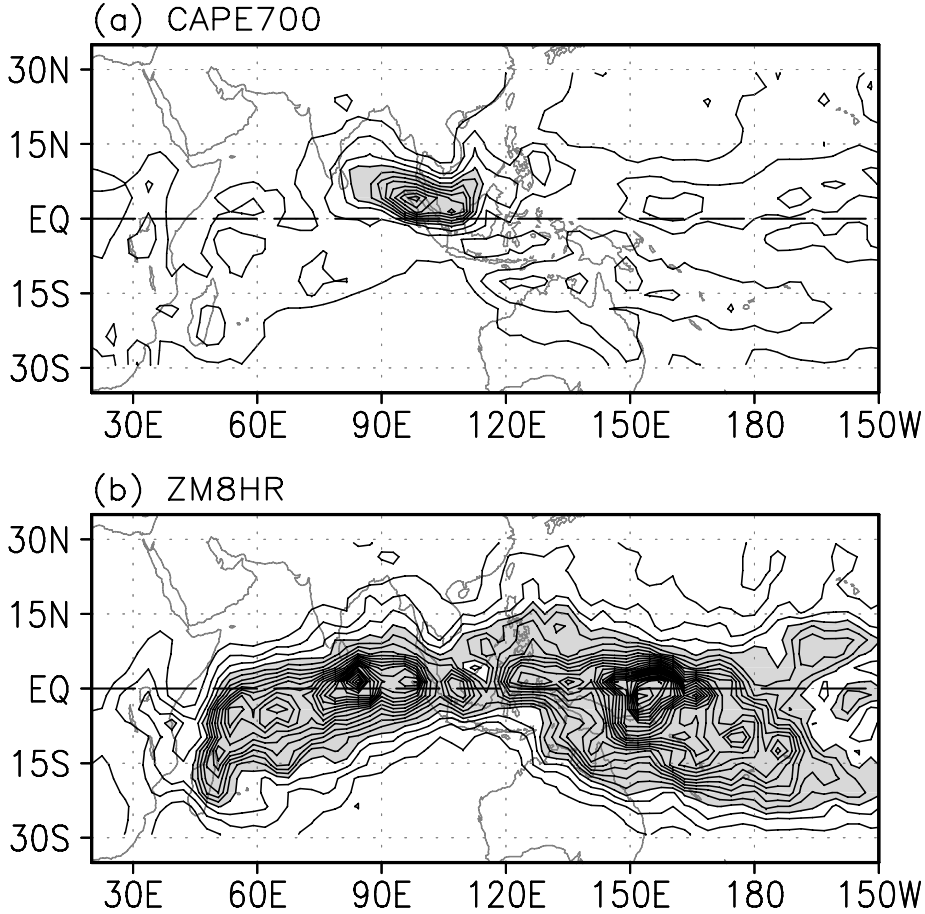

Fig. 5 Variance in 20-80-day filtered precipitation ($mm^2\ day^{-2}$) in (a) CAPE700 and (b) ZM8HR during DJFM averaged from 1979 to 2001. Contour is 5, $\geq$ 20 shaded.

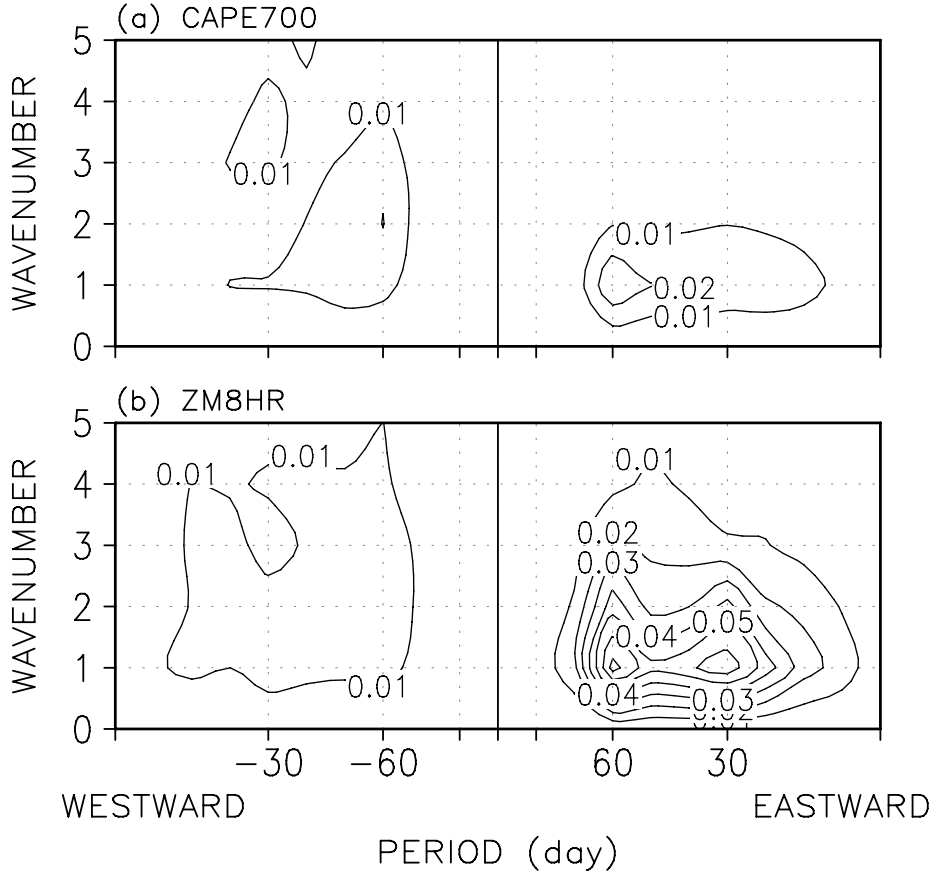

Fig. 6 Wave number power spectra in 850 hPa zonal wind (m^2 s^{-2}) in (a) CAPE700 and (b) ZM8HR during DJFM averaged from 1979 to 2001.

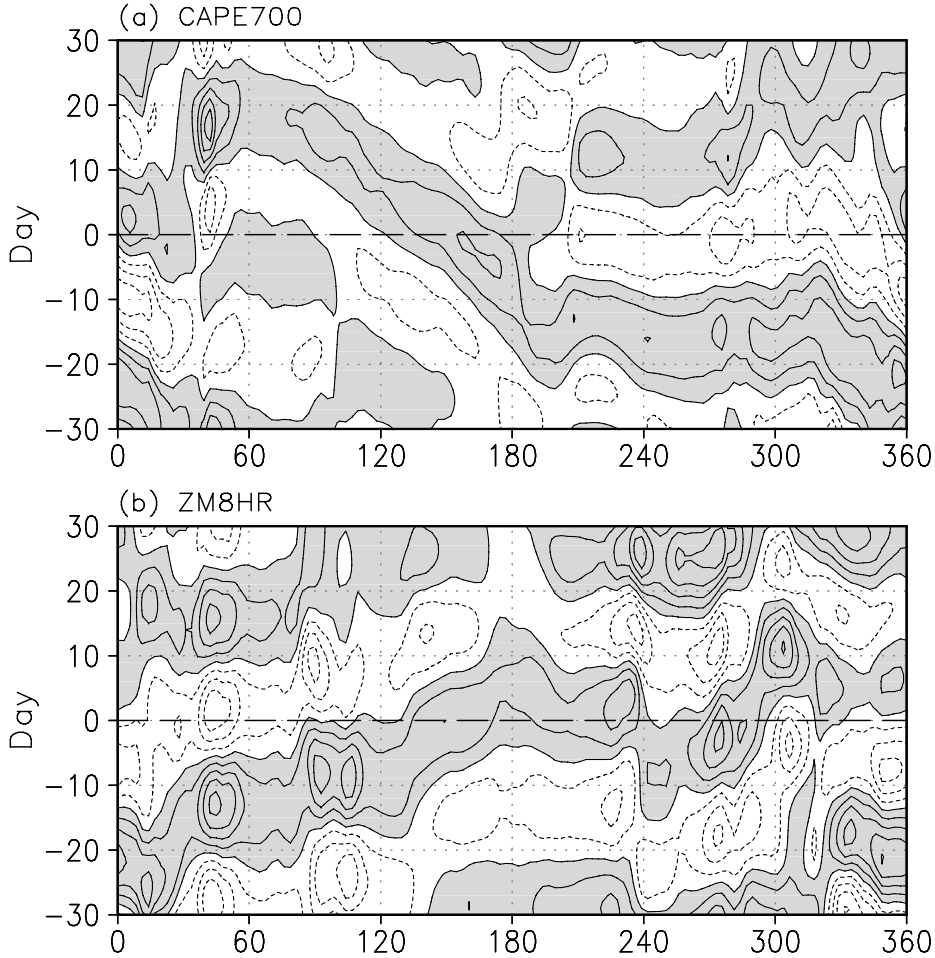

Fig. 7 Lag regression of filtered 850 hPa zonal wind (m s^{-1}) on 155°E in (a) CAPE700 and (b) ZM8HR during DJFM averaged from 1979 to 2001. Contour is 0.5, ≥ 0 shaded.

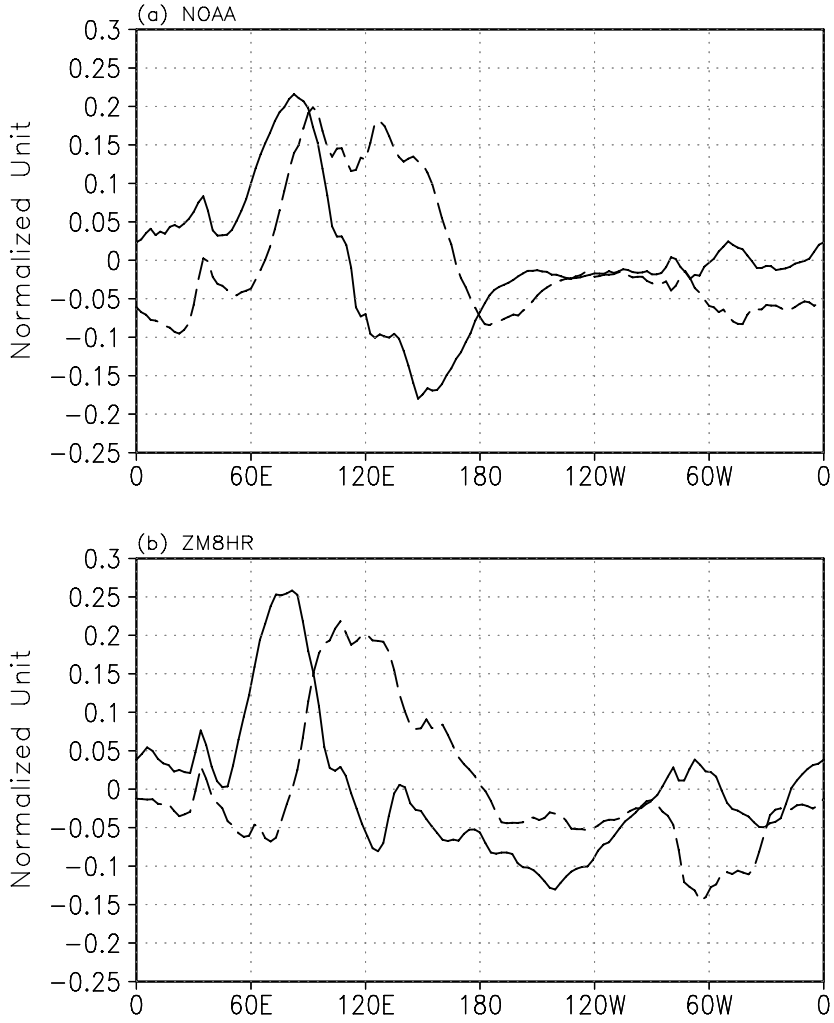

Fig. 8 EOF 1 (solid) and 2 (dashed) of the filtered OLR pentad anomaly along the equator (averaged in 10^{o}N~10^{o}S) from (a) NOAA satellite observation and (b) ZM8HR case in CAM3

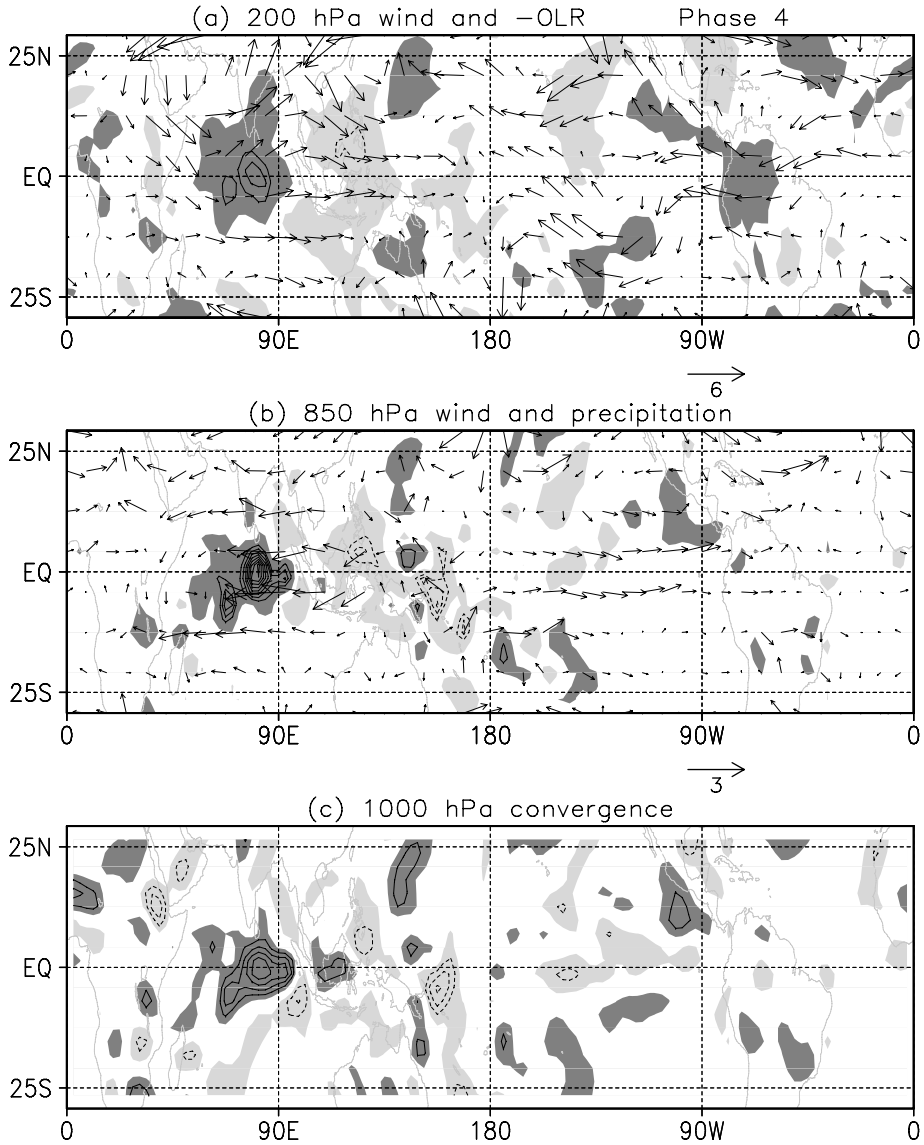

Fig. 9 Phase 4 of the composite MJO life cycle in ZM8HR case. (a) for 200 hPa wind anomalies (m s^{-1}) and –OLR (contour and shaded, W m^{-2}), contour interval is 5 with values in between (-10,10) omitted. (b) for 850 hPa wind anomalies (m s^{-1}) and precipitation (contour and shaded, mm day^{-1}), contour interval is 1 and values in (-2, 2) are omitted. (c) for 1000 hPa convergence (positive, $1x10^{-7}$ s^{-1}), contour interval is 5 and values in (-5, 5) are omitted. All darker shaded areas are for positive and lighter for negative.

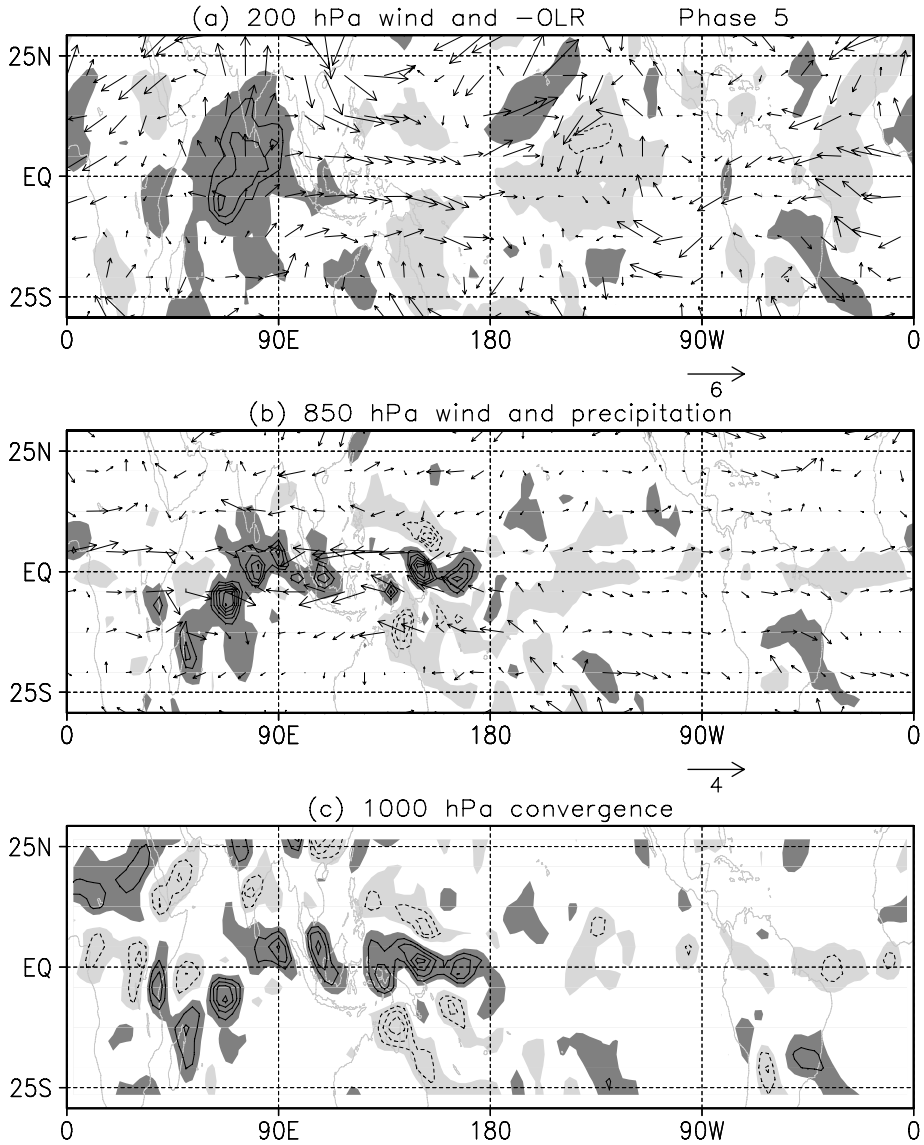

Fig. 10 Same as Figure 9 but for Phase 5.

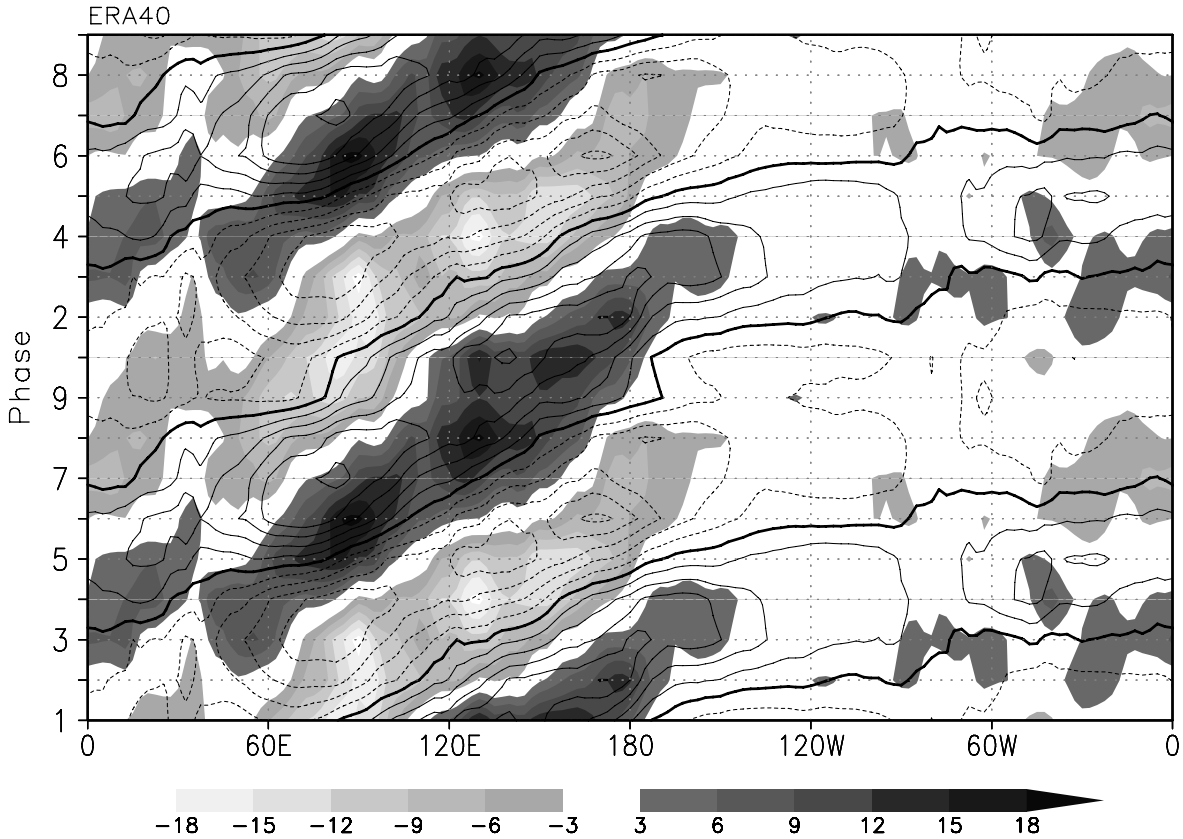

Fig. 11 Composite MJO life cycle in observational OLR (shaded) and 850 hPa zonal wind (contour) with interval 0.5 m s^{-1}

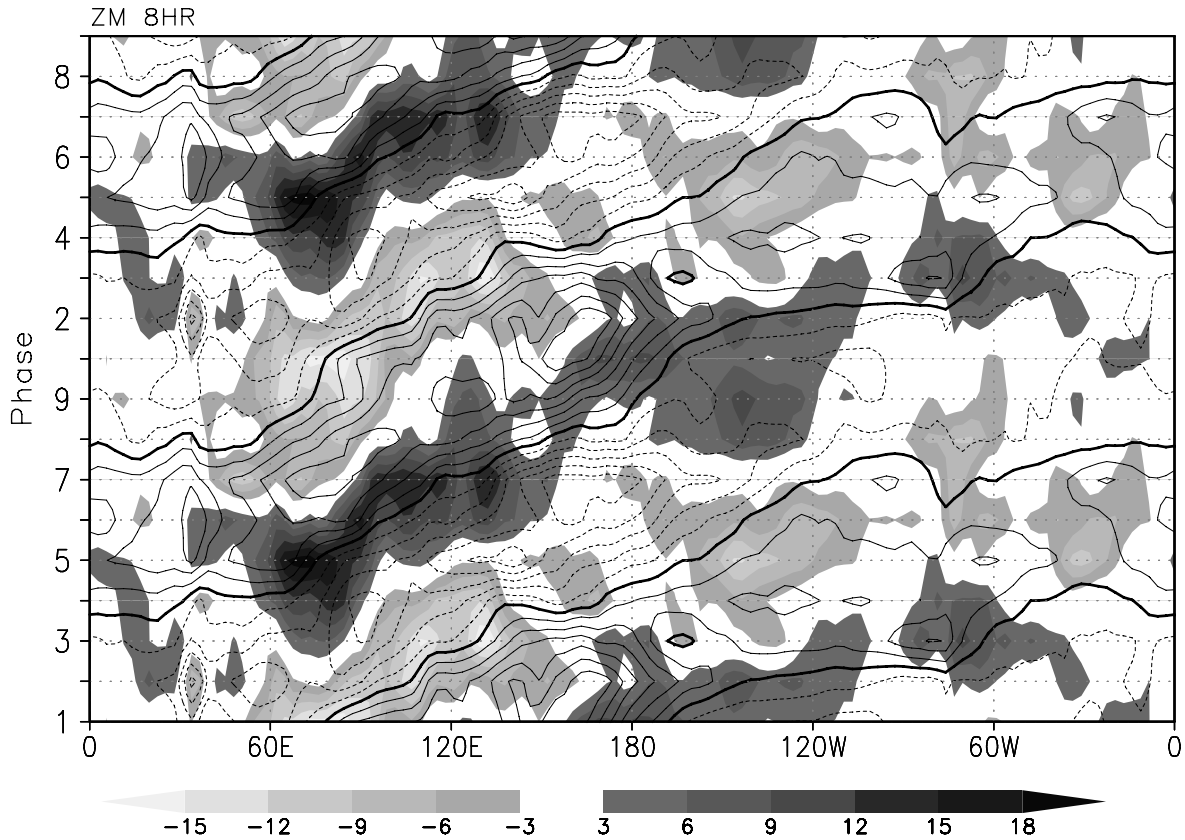

Fig. 12 Same as Figure 11 but for the ZM8HR case

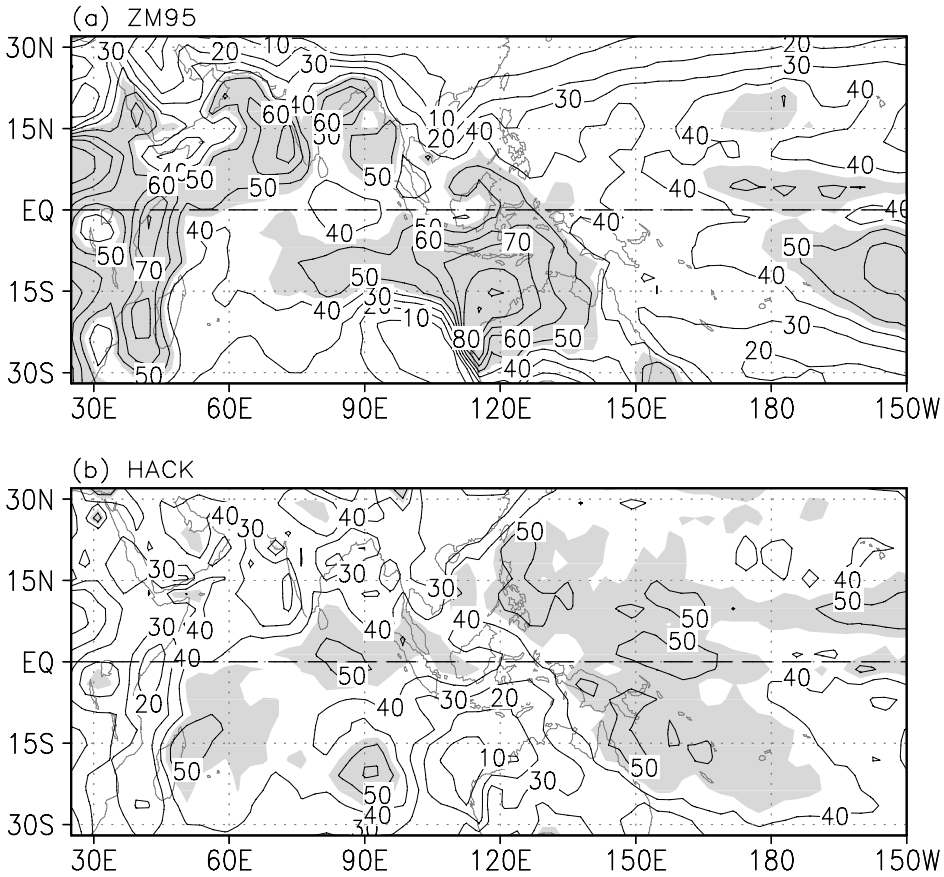

Fig. 13 Percentage of convective precipitation to the total in ZM8HR during DJFM season averaged from 1979 to 2001 for (a) deep ZM95 scheme and (b) shallow Hack scheme, ≥ 45% shaded.

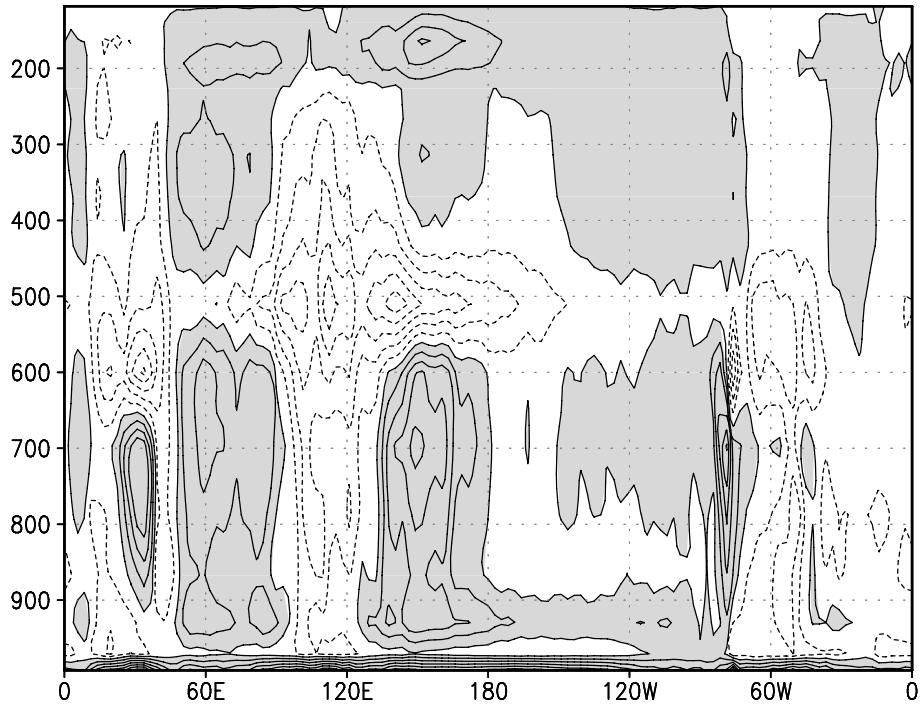

Fig. 14 Difference in total convective heating (deep + shallow, K day^{-1}), between ZM8HR and CTL during DJFM season averaged from 1979 to 2001 along the Equator (10^{o}N ~ 10^{o}S average). Contour interval is 0.5, $\geq$ 0 shaded.